

Supporting Information

Tailoring Vacancies Far Beyond Intrinsic Levels Changes the Carrier Type and Optical Response in Monolayer MoSe_{2-x} Crystals

Masoud Mahjouri-Samani,^{1} Liangbo Liang,¹ Akinola Oyedele,^{1,2} Yong-Sung Kim,^{1,3,4} Mengkun Tian,⁵ Nicholas Cross,⁵ Kai Wang,¹ Ming-Wei Lin,¹ Abdelaziz Boulesbaa,¹ Christopher M. Rouleau,¹ Alexander A. Puretzky,¹ Kai Xiao,¹ Mina Yoon,¹ Gyula Eres,⁶ Gerd Duscher,^{5,6} Bobby G. Sumpter,^{1,7} and David B. Geohegan¹*

¹Center for Nanophase Materials Sciences, Oak Ridge National Laboratory, Oak Ridge, TN, 37831, USA

²Bredesen Center for Interdisciplinary Research and Graduate Education, University of Tennessee, Knoxville, TN, 37996, USA.

³Korea Research Institute of Standards and Science, Daejeon 305-340, Korea

⁴Department of Nano Science, Korea University of Science and Technology, Daejeon 305-350, Korea

⁵Department of Materials Science and Engineering, University of Tennessee, Knoxville, TN, 37996, USA

⁶Materials Science and Technology Division, Oak Ridge National Laboratory, Oak Ridge, TN, 37831, USA

⁷Computer Science & Mathematics Division, Oak Ridge national Laboratory, Oak Ridge, TN 37831, USA

Correspondence Author

M. M-S Email: mahjourisamm@ornl.gov

DFT calculations for vibrational and Raman properties

Plane-wave DFT calculations were performed using the Vienna ab initio simulation package (VASP)¹ equipped with the projector augmented-wave (PAW) method for electron-ion interactions. Local density approximation (LDA) was adopted for the exchange-correlation interaction with the energy cutoff set at 300 eV, as LDA has been shown to yield excellent description of vibrational properties of 2D TMDs.^{2,3,4,5} Single-layer MoSe₂ systems were modeled by a periodic slab geometry, and a vacuum region of at least 18 Å in the out-of-plane direction was used to avoid spurious interactions with replicas. In the 2D slab calculations, all atoms were relaxed until the residual forces were below 0.001 eV/Å. For a primitive unit cell of pristine MoSe₂, its optimized in-plane lattice constant is 3.25 Å and Γ -centered 24×24×1 k-point samplings were used in the Monkhorst-Pack scheme.⁶ To model different Se vacancy concentrations in monolayer MoSe₂, supercells of different size were chosen with single or double Se atoms removed in each supercell. Specifically, we have considered a 4×4 supercell with a single Se vacancy (vacancy concentration 6.25%), a 4×4 supercell with a double Se vacancy (vacancy concentration 12.5%) and a 2×2 supercell with a single Se vacancy (vacancy concentration 25%). For each supercell, the atoms were re-optimized with fine k-point samplings until the residual forces were also below 0.001 eV/Å.

After each system was fully relaxed, the dynamic matrix was then calculated using the finite difference scheme implemented in the Phonopy software to obtain phonon frequencies and eigenvectors.^{7,8,9} Hellmann-Feynman forces in the supercell were computed by VASP for both positive and negative atomic displacements ($\delta = 0.03$ Å) and then used in Phonopy to construct the dynamic matrix, whose diagonalization provides phonon frequencies and phonon eigenvectors (i.e., vibrations). From the phonon eigenvectors, vibrations of each phonon mode can be visualized, which allows us to determine the A_g^1 vibrational mode in each defective system, and compare with the pristine system. In addition, non-resonant Raman intensity calculations were performed for the pristine system and the one with vacancy concentration 25%. Since Raman intensity $I \propto |e_i \cdot \tilde{R} \cdot e_s^T|^2$, the calculations of Raman tensors \tilde{R} are of most importance, which require information on phonon frequencies, phonon eigenvectors, and the

changes of dielectric tensors with respect to phonon vibrations. The derivatives of the dielectric tensors were also calculated by the finite difference approach. For both positive and negative atomic displacements in the single unit cell, the dielectric tensors were computed by VASP using density functional perturbation theory and then their derivatives can be obtained. With phonon frequencies, phonon eigenvectors, and derivatives of the dielectric tensors, the Raman tensors, \tilde{R} , can be computed. From this, the Raman intensity for every phonon mode is obtained for a given laser polarization set-up to finally yield a Raman spectrum after Gaussian broadening.

DFT calculations for electrical transport properties

To understand the mechanism behind the n- to p-type transition in the electrical transport measurements, we also performed first-principles calculations as implemented in VASP.¹⁰ The projector augmented wave (PAW) pseudopotentials,¹¹ the generalized gradient approximation (GGA) parametrized by Perdew, Burke, and Ernzerhof (PBE) for the exchange-correlation energy of electrons, and the kinetic energy cutoff of 350 eV were used.¹² The atomic structures were relaxed until the forces were less than 0.01 eV/Å. The $8 \times 8 \times 1$ Γ -centered k-point grid for the 1×1 monolayer MoSe₂ unit cell was used for the Brillouin-zone integration. The calculated hexagonal lattice constant of monolayer MoSe₂ is 3.312 Å. From the primitive unit cell of monolayer MoSe₂, we considered various different configurations of Se vacancies for the concentrations of 6.25% (one V_{Se} in 4×4 unit cell), 12.5% (two V_{Se} 's in 4×4 unit cell in all the possible configurations), and 25% (two V_{Se} 's in 2×4 unit cell in all the possible configuration).

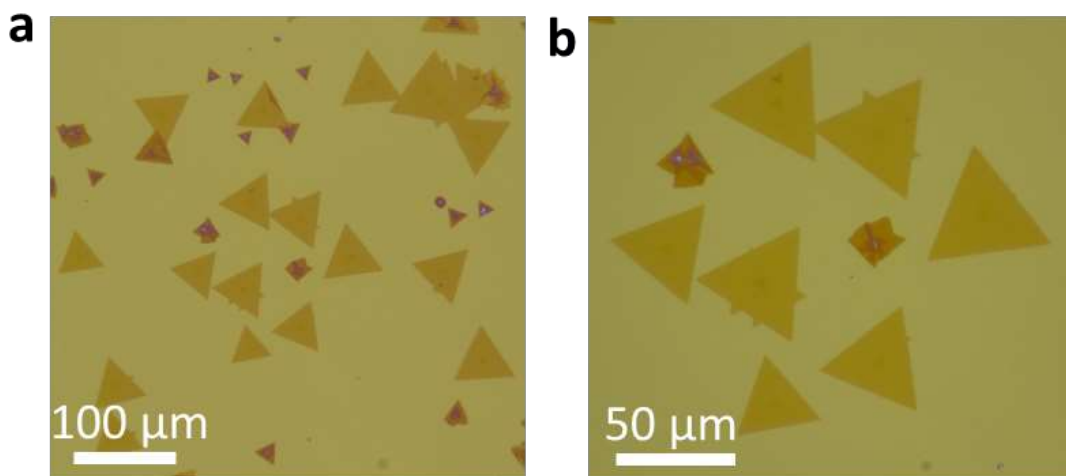


Figure S1. Optical microscope images of as-synthesized Se-deficient MoSe₂ crystals. (a, b) As synthesized highly Se-deficient MoSe₂ crystal imaged immediately after the growth process.

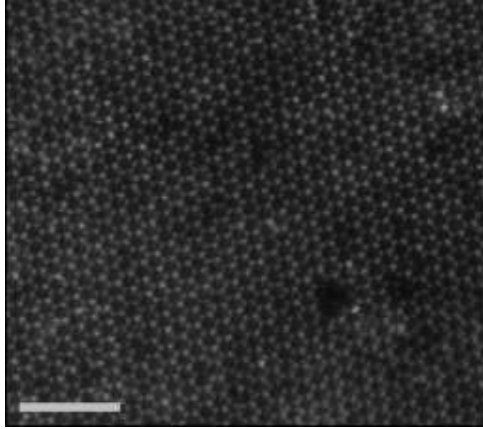


Figure S2. Atomic resolution STEM images show a partially repaired crystal after the post selenization process. After the post selenization process, most of the single vacancy sites are filled with Se atoms. However, after the healing process more double vacancies (holes) are observed in these samples, which could be due to degradation during handling and processing. Scale bar is 2 nm.

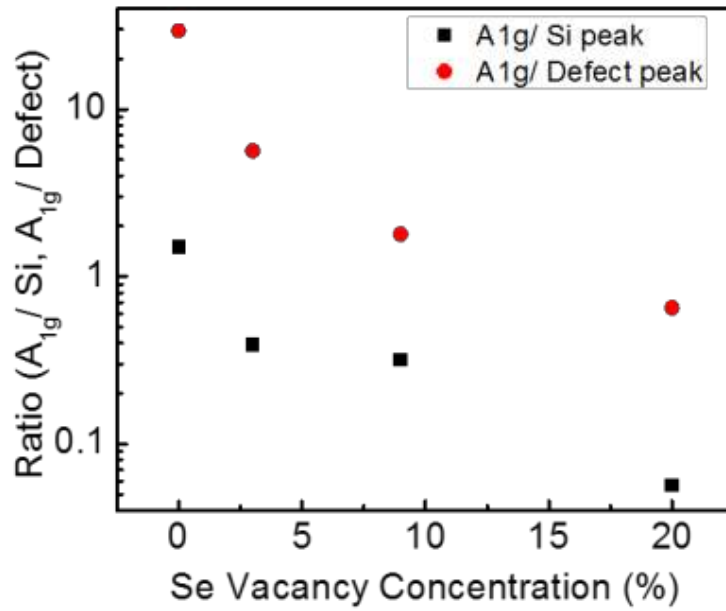


Figure S3. Raman peak ratios of MoSe₂ samples with different Se vacancy concentrations. The ratio of the A_{1g} peak intensity to the silicon peak intensity at 521 cm⁻¹ (black squares), and the ratio of A_{1g} peak intensity to the defect peak intensity at 250 cm⁻¹ for each spectrum in Fig. 2b.

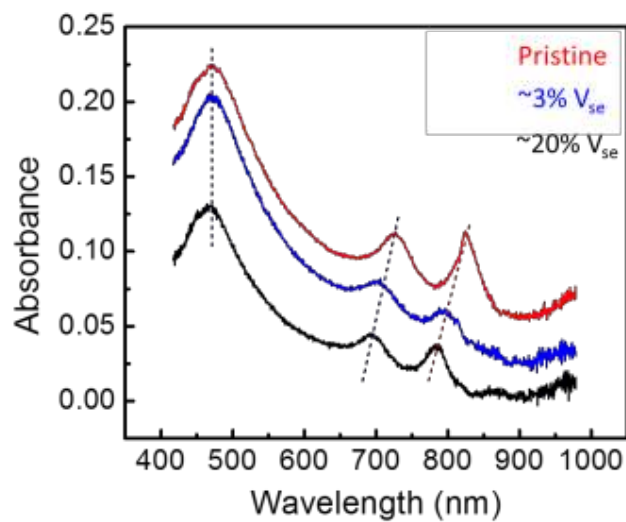


Figure S4. Evolution of absorption spectra of MoSe₂ as a function of Se vacancy concentration. Absorption spectra of the highly defective (~20% V_{se}), partially repaired (~3% V_{se}), and pristine samples. The crystals with higher vacancy concentration show a blue shift in their spectra compared to the pristine samples, and partially recover as they are post-selenized.

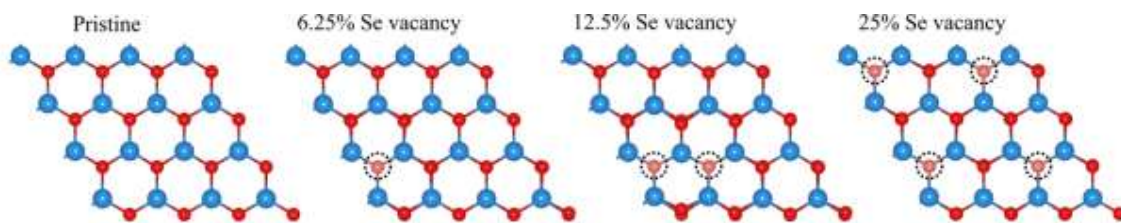


Figure S5. Atomic structures of monolayer MoSe₂ with different Se vacancy concentrations considered in the calculations. Blue (red) balls correspond to Mo (Se) atoms. The vacancy sites are highlighted by dashed circles and Se atoms at vacancy sites are shown in lighter red.

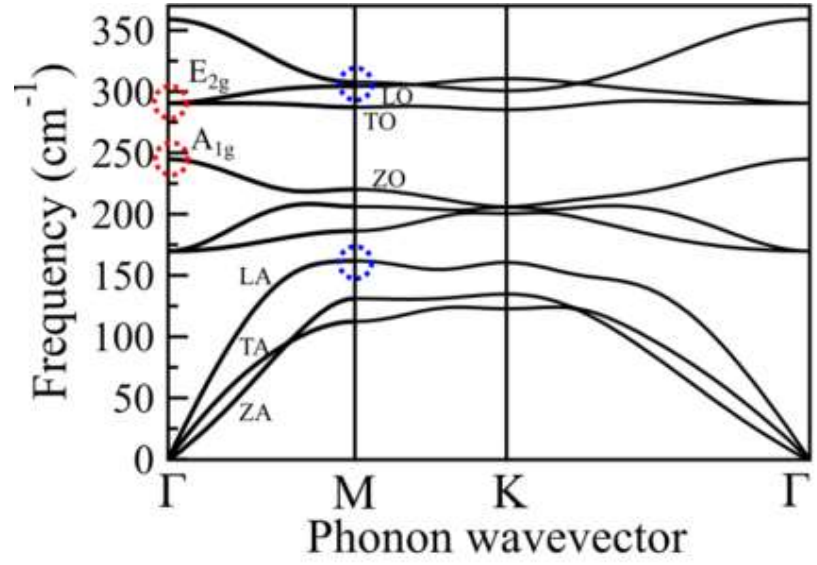


Figure S6. Phonon dispersion of pristine monolayer MoSe₂. The broad Raman peak around ~150 cm⁻¹ is probably from the LA phonon branch at the M point, referred as LA(M) as indicated by blue dash circle.

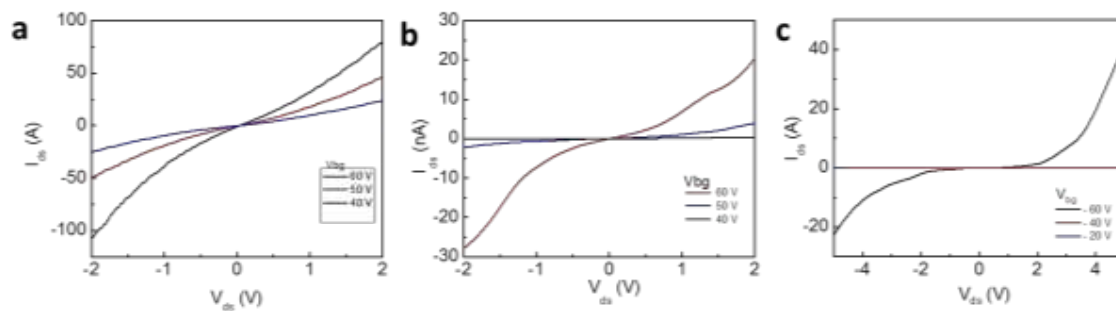


Figure S7. I-V curves of the MoSe₂ samples with low, moderate, and a high vacancy concentration. (a-c) I-V curves are measured from samples in Figure 3b-d, respectively.

References

1. Liang, L.; Meunier, V. *Nanoscale* **2014**, *6*, 5394–5401.
2. Zhao, Y. Y.; Luo, X.; Li, H.; Zhang, J.; Araujo, P. T.; Gan, C. K.; Wu, J.; Zhang, H.; Quek, S. Y.; Dresselhaus, M. S.; Xiong, Q. *Nano Lett.* **2013**, *13*, 1007-1015.
3. Huang, S.; Ling, X.; Liang, L.; Kong, J.; Terrones, H.; Meunier, V.; Dresselhaus, M. S. *Nano Lett.* **2014**, *14*, 5500-5508.
4. Molina-Sánchez, A.; Wirtz, L. *Phys. Rev. B* **2011**, *84*, 155413.
5. Puretzky, A. A.; Liang, L.; Li, X.; Xiao, K.; Wang, K.; Mahjouri-Samani, M.; Basile, L.; Idrobo, J. C.; Sumpter, B. G.; Meunier, V.; Geohegan, D. B. *ACS Nano* **2015**, *9*, 6333–6342.
6. Monkhorst, H. J.; Pack, J. D. *Phys. Rev. B* **1976**, *13*, 5188-5192.
7. Togo, A.; Oba, F.; Tanaka, I. *Phys Rev B* **2008**, *78*, 134106.
8. Liang, L.; Meunier, V. *Appl. Phys. Lett.* **2013**, *102*, 143101.
9. Ling, X.; Liang, L.; Huang, S.; Puretzky, A. A.; Geohegan, D. B.; Sumpter, B. G.; Kong, J.; Meunier, V.; Dresselhaus, M. S. *Nano Lett.* **2015**, *15*, 4080–4088.
10. Kresse, G. & Furthmuller, J. Efficient iterative schemes for ab initio total-energy calculations using a plane-wave basis set. *Phys. Rev. B* **1996**, *54*, 11169-11186.
11. Blochl, P.E. Projector augmented-wave method. *Phys. Rev. B* **1994**, *50*, 17953-17979.
12. Perdew, J.P., Burke, K. & Ernzerhof, M. Generalized Gradient Approximation Made Simple. *Phys. Rev. Lett.* **1996**, *77*, 3865-3868.